Applied Catalysis B: Environmental 115–116 (2012) 45–52

Contents lists available at SciVerse ScienceDirect

Applied Catalysis B: Environmental

journal homepage: www.elsevier.com/locate/apcatb

Investigation of iron oxide reduction by ethanol as a potential route to produce hydrogen

M.G. Rosmaninho[a], F.C.C. Moura[a], L.R. Souza[a], R.K. Nogueira[a], G.M. Gomes[a], J.S. Nascimento[a], M.C. Pereira[a], J.D. Fabris[a], J.D. Ardisson[b], M.S. Nazzarro[c], K. Sapag[c], M.H. Araújo[a], R.M. Lago[a,*]

[a] Departamento de Química, ICEx, Universidade Federal de Minas Gerais UFMG, 31270-901 Belo Horizonte, MG, Brazil
[b] Laboratório de Física Aplicada, Centro de Desenvolvimento e Tecnologia Nuclear (CDTN), Belo Horizonte, 31270-901, MG, Brazil
[c] Laboratorio de Ciencias de Superficies y Medios Porosos, Dpto de Física, UNSL, San Luis, Argentina

ARTICLE INFO

Article history:
Received 28 March 2011
Received in revised form 13 July 2011
Accepted 21 November 2011
Available online 30 November 2011

Keywords:
Hydrogen production
Hydrogen storage
Ethanol
Iron oxide

ABSTRACT

In this work, a novel way to indirectly store and produce H_2 from ethanol was investigated using a two-step process based on the reduction of iron oxide followed by oxidation with H_2O. The reduction of different iron oxides, i.e., Fe_2O_3, Fe_3O_4 and FeOOH, with ethanol to produce Fe^o was investigated. TPRe (Temperature Programmed Reactions) and Mössbauer and XRD analyses showed that ethanol reduces Fe_2O_3 sequentially to Fe_3O_4 at 350–500 °C, to Fe_3O_4/FeO at 500–600 °C and finally to Fe^o at 700 °C. The formed Fe^o can then be oxidized by H_2O to produce H_2 and Fe_3O_4, as shown by Mössbauer and XRD analyses. Cyclic experiments showed that iron could be consecutively reduced/oxidized at least 5 times without any significant decrease in H_2 production after the second cycle. However, reactions of Fe_2O_3 with ethanol at higher temperatures, i.e., 800 and 900 °C, led to the formation of iron carbide and significant carbon deposition. XPS, SEM, TEM, Raman and TG showed 24–28 wt% carbon content, particularly on the surface as nanofibers and as amorphous and graphitic carbon.

1. Introduction

Different methods for the production of hydrogen fuel have been investigated in recent years, e.g., electrolysis [1–3], thermolysis [4–6], water photolysis [7,8], biological processes [9–11] and reforming of methane or alcohols [12–15]. Nevertheless, the utilization of hydrogen in fuel cell vehicles still faces several fundamental problems, such as the cost of production and the safety and efficiency of storage [16–18].

Hydrogen production from ethanol has gained much attention worldwide in the last decade. Ethanol is a renewable and increasingly available feedstock. It is easy to transport, biodegradable, low in toxicity and free from catalyst poisons such as sulfur [13,15,19,20].

Hydrogen can be produced directly from ethanol using different processes, such as steam reforming (Eq. (1)), using a catalyst, e.g., Rh, Ru, Pd, Co or Ni, on a support. Possible supports include Al_2O_3, CeO_2, MgO, ZnO and La_2O_3 [19–22]. Autothermal reforming has also been investigated and combines steam reforming with the partial oxidation of ethanol (Eq. (2)) [20,23–25]. Several studies have reported different catalysts for the autothermal reforming of ethanol, e.g., Rh–Ce [24], $Cu_{1-x}Ni_xZnAl$-mixed metal oxides [26,27], Pt/Al_2O_3 [14], Ni·Rh/CeO_2 [28–30], Ni/M_xO_y·Al_2O_3 [31–34] and Pd, Co and Mn/ZnO [35,36].

Finally, the catalytic partial oxidation of ethanol (Eq. (3)) in the presence of Cu [37,38], Co [39,40], Fe, Ni [40,41], or noble metals [39,42] has also been used to produce hydrogen.

$$C_2H_5OH + 3H_2O \rightarrow 2CO_2 + 6H_2 (\Delta H^\circ_{298} = +174\,kJ\,mol^{-1}) \quad (1)$$

$$C_2H_5OH + 1/2O_2 + 2H_2O \rightarrow 2CO_2 + 5H_2 (\Delta H^\circ_{298} = -50\,kJ\,mol^{-1}) \quad (2)$$

$$C_2H_5OH + 1/2O_2 \rightarrow 2CO_2 + 3H_2 \quad (\Delta H^\circ_{298} = +20\,kJ\,mol^{-1}) \quad (3)$$

This work proposes the use of a new system based on a reversible redox cycle involving iron oxide and iron metal to produce hydrogen from ethanol. In the first step, ethanol reduces the iron oxide (e.g., Fe_2O_3) to iron metal. In the second step, H_2 is produced by the oxidation of the iron metal with water (Fig. 1). An important potential advantage of this process is the indirect storage of hydrogen. The iron metal obtained in the first part of the cycle can be stored and transported to produce H_2 wherever it is necessary.

An iron redox system has been previously investigated to produce high-purity hydrogen for a polymer electrolyte fuel cell (PEFC) based on the Steam-Iron Process (SIP), which was originally used to

* Corresponding author.
E-mail address: rochel@ufmg.br (R.M. Lago).

0926-3373/$ – see front matter © 2012 Published by Elsevier B.V.
doi:10.1016/j.apcatb.2011.11.038

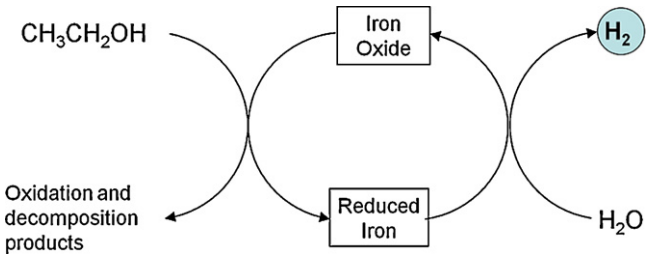

Fig. 1. Iron-based redox system to produce hydrogen from ethanol.

purify hydrogen produced by gasified coal [43–50]. In such a system, impure hydrogen containing CO is used to reduce iron oxide to Fe^o (Eqs. (4) and (5)), which then reacts with steam to produce pure H_2 (Eq. (6)). Several recent studies have investigated the use of iron oxides modified by the addition of different metals, e.g., Al, Ti, Cr, Ga or Mo, to mitigate the sintering of iron oxides and/or iron metal during the repeated redox cycles. The addition of metals such as Cu, Ni, Pt and Rh promoted the reactivity of the iron oxides in the redox reaction at lower temperatures [45,46,51–53].

$$Fe_3O_4 + 4H_2 \rightarrow 3Fe^o + 4H_2O \quad (4)$$

$$Fe_3O_4 + 4CO \rightarrow 3Fe^o + 4CO_2 \quad (5)$$

$$Fe^o + 4H_2O \rightarrow Fe_3O_4 + 4H_2 \quad (6)$$

One advantage of the process described in the present work compared to SIP is that it does not need the reforming step to produce syngas, i.e., ethanol directly reduces the iron oxides.

Herein, we describe the results obtained for the reaction of ethanol with different iron oxides, i.e., α-Fe_2O_3, Fe_3O_4 and γ-FeOOH. A detailed investigation of the formation of carbon and preliminary studies on the oxidation of Fe^o by steam to produce H_2 are also presented.

2. Experimental

Iron oxides synthesis: goethite (γ-FeOOH), hematite (α-Fe_2O_3), and magnetite (Fe_3O_4).

Hematite was produced by the thermal treatment of $Fe(NO_3)_3{\cdot}9H_2O$ at 450 °C for 3 h under atmospheric air. Magnetite was prepared by the thermal decomposition of the precursor, iron hydroxyl-acetate $[Fe(CH_3COO^-)_x(OH)_{3-x}]$, at 400 °C for 2 h under N_2 (at a flow rate of 30 mL min^{-1}). Goethite was synthesized by the precipitation of iron hydroxide from a $FeCl_3$ solution (1 mol L^{-1}) using potassium hydroxide (5 mol L^{-1}) at 70 °C, followed by aging for 60 h.

2.1. Temperature programmed reactions – TPRe

The reduction reaction with ethanol and the oxidation reaction with water (hydrogen production) were performed as described below.

In the reactions with ethanol, nitrogen was used as a carrier gas (30 mL min^{-1}) and was saturated with ethanol at 0 °C. Under these conditions, ethanol has a vapor pressure of 11.8 mmHg, corresponding to an ethanol concentration in the gas stream of 1.6% or 0.7 μmol mL^{-1}.

In the reaction with water, N_2 (30 mL min^{-1}) was also used as a carrier gas and was saturated with water at 28 °C. Under these conditions, water has a vapor pressure of 23.8 mmHg, corresponding to a water concentration in the gas stream of 3.2% or 1.4 mol mL^{-1}.

Approximately 30 mg of the iron oxide were placed in a quartz tube that was heated in a tubular furnace (Lindberg BLUE M) to different temperatures (300–900 °C) at 5 or 10 °C min^{-1} and held at the final temperature for 0–4 h.

The reaction products were analyzed online using a GC Shimadzu 17A equipped with a flame ionization detector (FID) or using a TPR instrument (ChemBET3000, Quantachrome Instruments) with a thermal conductivity detector (TCD).

After the reaction with ethanol, all of the samples were cooled to room temperature under a N_2 flow and immediately drenched in mineral oil to avoid any oxidation of the iron phases by oxygen from the air.

2.2. Characterization

Mössbauer spectroscopic analyses were performed in a CMTE spectrometer (model MA250) using a cobalt-57 source in a rhodium matrix (^{57}Co/Rh) and α-Fe as reference. The spectra were analyzed using the Normos-90 software.

X-ray diffraction (XRD) analyses were performed in a Philips XPW-1830 using either Cu (0.154 nm) or Co (0.179 nm) radiation.

Surface areas were determined by nitrogen adsorption by the BET method using an Autosorb-1 from Quantachrome Instruments.

Scanning electronic microscopy (SEM) images were obtained using a Joel JSM 840A instrument using a current of 6×10^{-11} A, an acceleration voltage of 15 kV and a pressure of 5×10^{-7} torr. Transmission electron microscopy (TEM) images were obtained using a Tecnai – G2-20-FEI 2006 microscope operating with 200 kV.

Thermal analyses were performed in a Shimadzu TGA60 simultaneous TG/DTA instrument using an alumina pan, an air flow rate of 100 mL min^{-1} and temperatures of 25–900 °C with a heating rate of 10 °C min^{-1}.

X-ray photoelectron spectra (XPS) were acquired with a VG Escalab 200R spectrometer equipped with a hemispherical electron analyzer and a Mg Kα ($h\upsilon$ = 1253.6 eV) X-ray source. The sample was first placed in a small stainless-steel holder that was mounted on a sample rod in the pretreatment chamber of the spectrometer and then degassed at room temperature and 10^{-5} mbar for 5 h prior to being transferred to the analysis chamber. The residual pressure was maintained below 3×10^{-8} mbar. The binding energies (BE) were referenced to the C 1s peak (284.9 eV) to account for the charging effects.

The saturation magnetization measurements were performed in a portable magnetometer with a permanent Nd–Fe–B magnet with a fixed magnetic field of 0.3 Tesla. The Raman analyses were performed in an IN Via Renishaw micro-Raman system with a 514.5 nm laser.

3. Results and discussion

3.1. Characterization of pure iron oxides

Different iron oxides, i.e., α-Fe_2O_3 (hematite), Fe_3O_4 (magnetite) and γ-FeOOH (goethite), were investigated for the reaction with ethanol. These Fe oxides were characterized by XRD and Mössbauer spectroscopy. The XRD analysis (Supplementary Material) showed the presence of pure crystalline phases with an average crystallite size of 23, 29 and 12 nm for hematite, magnetite and goethite, respectively.

Mössbauer spectra (Supplementary Material) showed simple sextets, suggesting the presence of pure phases for hematite and goethite and confirming the XRD results. For magnetite, two signals were observed that are associated with the octahedric and tetrahedric sites with an approximate 2:1 ratio, indicating the presence of nearly stoichiometric Fe_3O_4. The Mössbauer hyperfine parameters and the crystallite size (determined by XRD) of the different iron oxides are shown in the Supplementary Material.

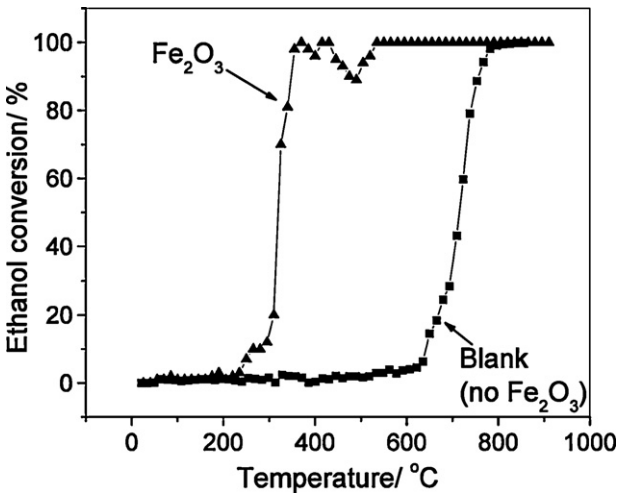

Fig. 2. TPRe curves showing the conversion of ethanol in presence of α-Fe_2O_3 and in the absence of iron oxide (blank).

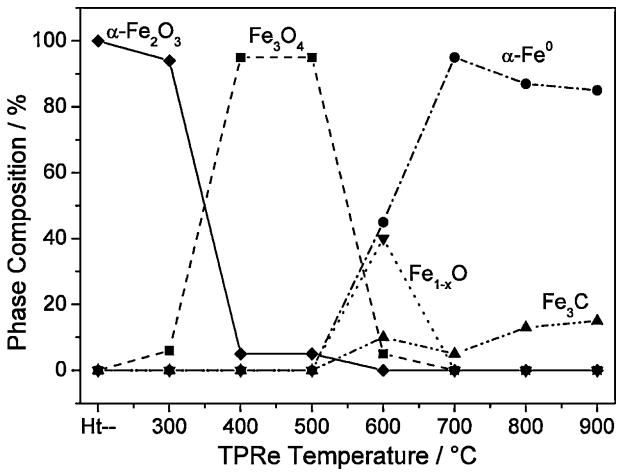

Fig. 3. Phase composition obtained by Mössbuer spectra of hematite after the TPRe with ethanol at different temperatures.

3.2. TPRe with ethanol and hematite

The reactions of hematite with ethanol were investigated using a TPRe (Temperature Programmed Reaction) up to 900 °C. Fig. 2 shows the TPRe curves obtained in the presence of α-Fe_2O_3 and in the absence of iron oxide (a blank experiment).

It can be observed in the blank experiment that ethanol is converted only at temperatures higher than 600 °C and is mainly converted to ethene, which is likely produced by intramolecular dehydration.

In the presence of α-Fe_2O_3, ethanol is completely converted at temperatures as low as 250–300 °C. At low temperatures, ethene, acetaldehyde and small amounts of other products (methanol and formaldehyde) were detected; this is likely due to the oxidation of ethanol by oxygen from the oxide structure. At higher temperatures, only very small amounts of these oxidized organic molecules were observed (Supplementary Material).

To investigate the different reactions of hematite during the TPRe, the reactor was quenched at different temperatures and the solid was subsequently analyzed by Mössbauer spectroscopy, XRD and XPS.

It can be observed in the Mössbauer spectra (Supplementary Material) that hematite is gradually reduced by ethanol. At 400–500 °C, the hematite was almost completely reduced to magnetite. At 600 °C, some wüstite can be detected, but at 700 °C the main phase present is metallic iron. At higher temperatures, i.e., 800 and 900 °C, iron carbide (Fe_3C) is formed. A general idea of the Fe phase compositions after the reaction with ethanol at different temperatures is given in Fig. 3. Measurements of the saturation magnetization showed values of 18, 49, 60, 51 and 49 $J T^{-1} kg^{-1}$ for α-Fe_2O_3 after the TPRe at 350, 600, 700, 800 and 900 °C, respectively (before the TPRe, the hematite had a saturation magnetization of 0 $J T^{-1} kg^{-1}$). These results completely agree with the Fe composition; at 350 °C, magnetite is formed and some magnetism is conferred to the sample, whereas at 700 °C, Fe metal is primarily produced and a high saturation magnetization results. For the samples obtained at 800 and 900 °C, some Fe metal is converted to the non-magnetic phase Fe_3C, which leads to a decrease in the magnetization.

XRD (not shown) confirmed the Mössbauer results and suggested an average particle size of Fe^o of 46 and 45 nm after reduction at 700 and 800 °C, respectively.

Based on these results, a simple assignment of the hematite reactions with ethanol on the TPRe curve can be proposed (Fig. 4).

The GC analyses show a small amount of ethanol consumption below 300 °C, which is likely related to the beginning of the reaction with hematite where a non-stoichiometric partially reduced oxide, e.g., Fe_2O_{3-x}, is produced. From 300 to 400 °C, the ethanol in the gas stream is completely consumed due to the reduction of hematite to magnetite. From 400 to 550 °C, there are varying amounts of ethanol at low concentrations, suggesting a complex reaction. Most likely, the production of magnetite is still the main reaction that is taking place because Fig. 3 shows that, at this temperature, Fe_3O_4 is the main phase present. However, above 500 °C, Fe_3O_4 is primarily reduced to Fe^o, with some FeO (wüstite) also formed. Above 700 °C, carbon deposition takes place, and the reaction of carbon with Fe^o results in the formation of iron carbide (Fe_3C).

The TPRe was also used to investigate the reaction of ethanol with Fe_3O_4 and γ-FeOOH. The ethanol consumption is shown in Fig. 5.

Hematite and goethite begin the conversion of ethanol at a similar temperature, ca. 300 °C. This similar behavior is likely related to the dehydration of goethite below 300 °C to form hematite [54]. The conversion of ethanol in the presence of magnetite occurs only at higher temperatures, ca. 350 °C. This is likely related to the stability of Fe_3O_4, which requires higher temperatures for its reduction compared to Fe_2O_3 [55,56]. It was interesting to observe that all

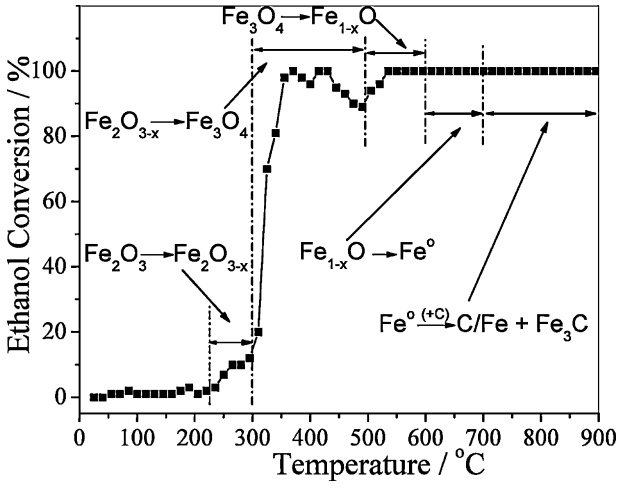

Fig. 4. Reduction of the Fe phases with ethanol as a function of the temperature in a TPRe curve.

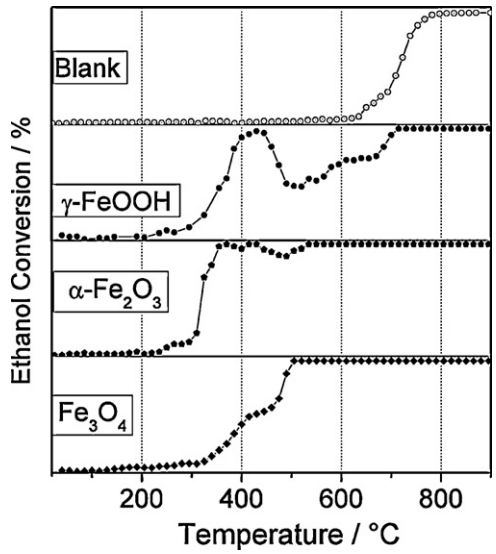

Fig. 5. Ethanol conversion during the TPRe experiment in the presence of α-Fe_2O_3, Fe_3O_4 and γ-FeOOH.

the Fe oxides will react by a common route starting from α-Fe_2O_3 or γ-FeOOH to form Fe_3O_4 and then FeO and Fe^o.

The iron products obtained after the TPRe reached 900 °C for α-Fe_2O_3, Fe_3O_4 and γ-FeOOH were analyzed by Mössbauer spectrometry and XRD. The Mössbauer spectra and XRD diffratograms (Figs. 6 and 7) showed that after the TPRe reached 900 °C, only two iron phases remained: metallic iron (α-Fe^o) and iron carbide (Fe_3C). The hematite and magnetite precursors showed similar amounts of metallic Fe (80–85%), whereas goethite produced significantly less Fe^o (ca. 56%). Although the reason for this behavior is not clear, it is likely related to the smaller particle size observed for goethite. These smaller particles are more reactive and could react more easily with ethanol or any deposited carbon to produce iron carbide.

The powder X-ray diffractograms for α-Fe_2O_3 and Fe_3O_4 after the TPRe with ethanol reached 900 °C are shown in Fig. 7.

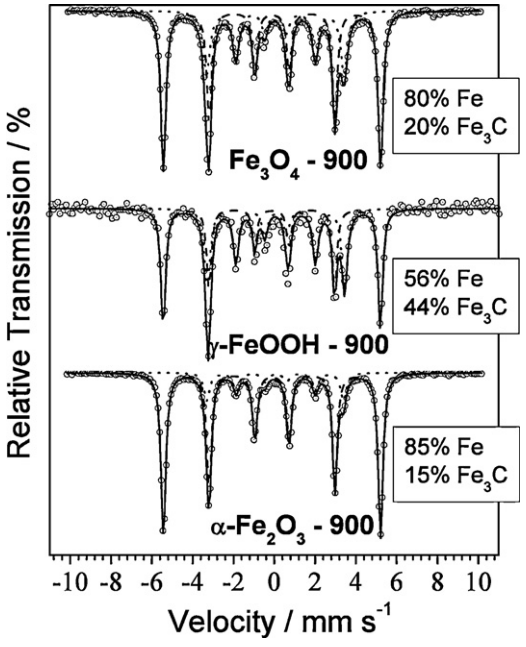

Fig. 6. Mössbauer spectra obtained and iron phases observed after the TPRe of the different iron oxides reached 900 °C with ethanol.

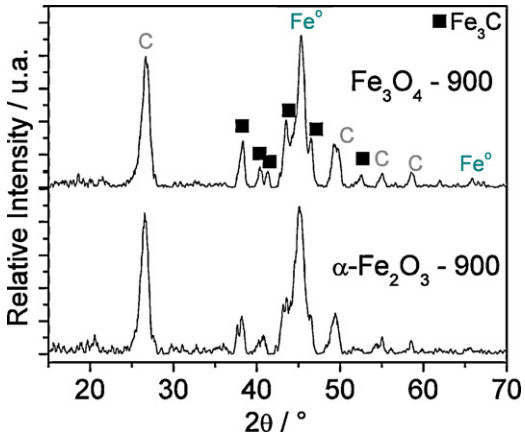

Fig. 7. X-ray diffratograms obtained after the TPRe of α-Fe_2O_3 and Fe_3O_4 reached 900 °C with ethanol.

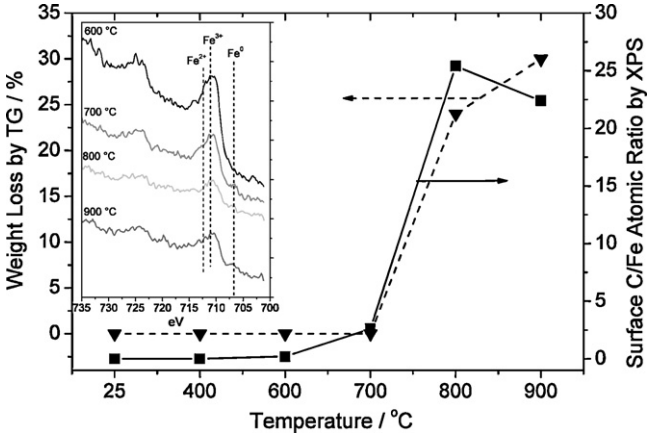

Fig. 8. Weight loss (by TG) and surface C/Fe atomic ratios (by XPS) for hematite after reaction with ethanol at different temperatures. A typical XPS spectrum is shown in the detail.

Average Fe^o crystallite sizes of 7 and 13 nm were obtained for hematite and magnetite, respectively, after the TPRe reached 900 °C, whereas the Fe_3C crystallite sizes were ca. 10 nm. The peak at 2θ ca. 27° indicates the presence of graphitic structures with crystallite sizes of ca. 9 nm. In fact, the TG/DTA analyses (Supplementary Material) performed in air showed that exothermic weight losses at temperatures above 600 °C were likely related to the oxidation of carbon. According to these weight losses, a carbon content of approximately 24 and 28 wt% was calculated for α-Fe_2O_3 after the

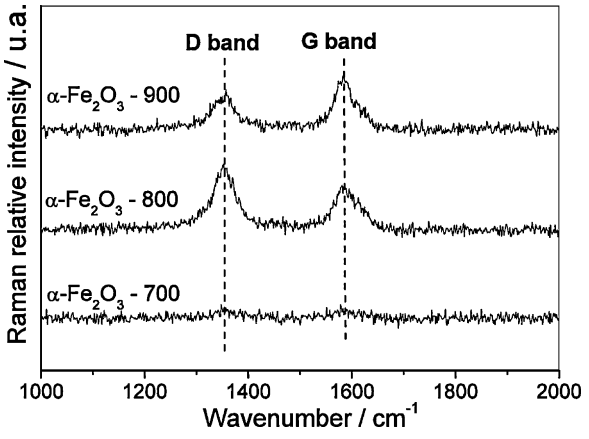

Fig. 9. Raman spectra for hematite after the TPRe at 700, 800 and 900 °C.

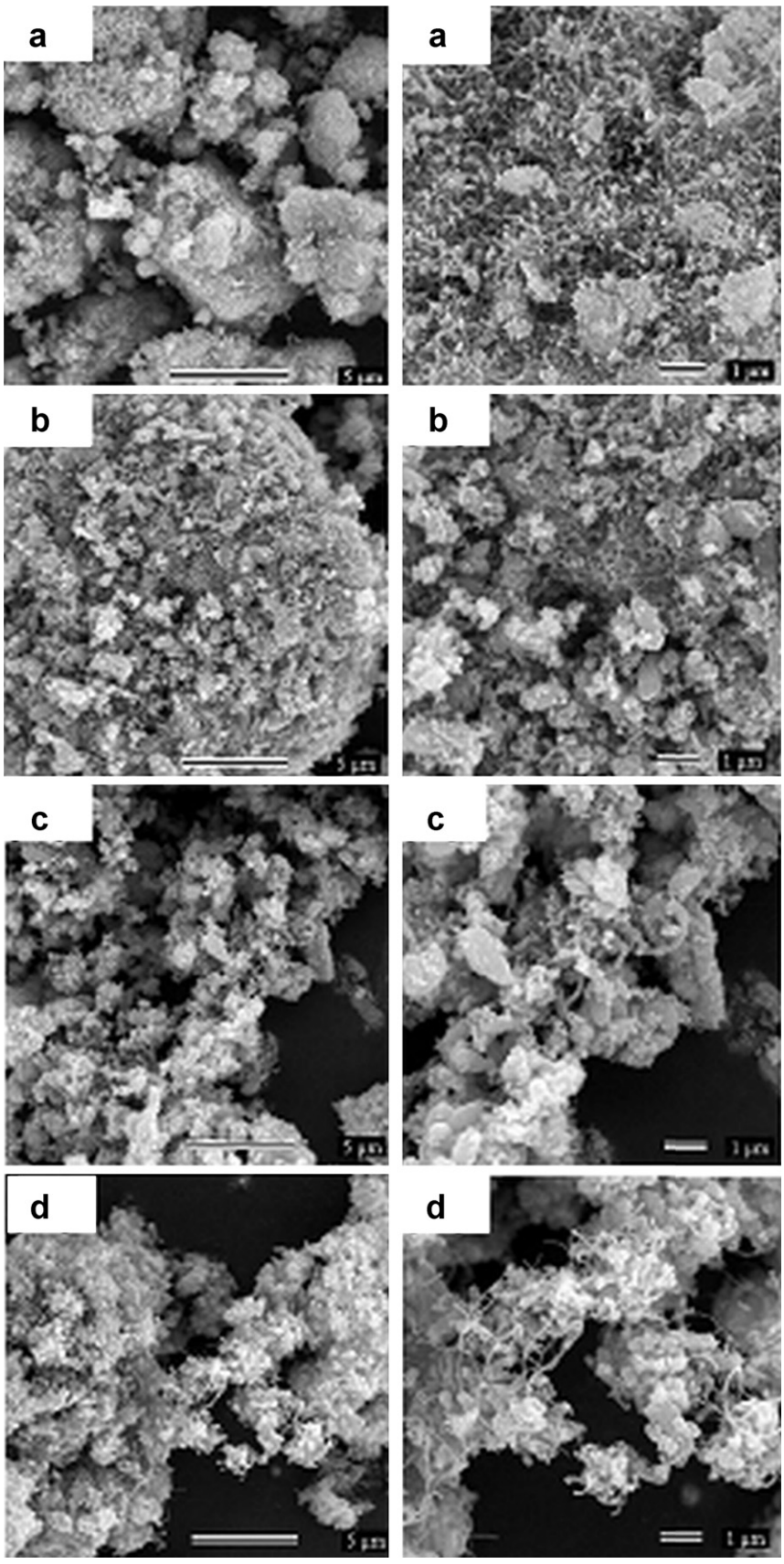

Fig. 10. SEM images of Fe_2O_3 (a) before and (b–d) after the TPRe at (b) 600 °C, (c) 700 °C and (d) 900 °C.

TPRe reached 800 and 900 °C, respectively. On the other hand, a TG analysis of the same sample after the TPRe was performed at 700 °C did not show any significant amount of carbon.

The carbon deposition on the iron surface was also investigated by XPS analyses. Fig. 8 shows a typical spectrum (detail) and the C/Fe surface ratio.

XPS spectra showed signals at binding energies (BEs) of 724 and 711 eV that were related to Fe $2p_{1/2}$ and Fe $2p_{3/2}$, respectively. These peaks were probably related to oxidized species (i.e., Fe_3O_4) and iron carbide. The analysis of the different species of iron from the Fe 2p peaks is difficult due to the very similar binding energies. On the other hand, the intensities of these peaks decrease with the reaction temperature, which is probably due to the consumption of the oxidized phases to form Fe^o at higher temperatures (Fe $2p_{3/2}$ at BE 707 eV). In all of the samples, a broad peak of C 1 s occurs at BE 283–286 eV and could be associated with the presence of different carbon species (i.e., amorphous carbon, graphite and iron carbide) [57–61].

From the surface atomic C/Fe ratio obtained by the integration of the XPS signals of C 1s and Fe 2p after the TPRe at different temperatures, it can be observed that the C/Fe ratio is close to 0 up to 600 °C (when the background carbon signal is taken into consideration). At 700 °C, a small increase in the C/Fe surface ratio is observed. At 800–900 °C, a remarkable increase is observed in the C/Fe ratio as it reaches ca. 25. For a surface atomic ratio of 25, a composition of 85 wt% carbon and only 15 wt% Fe would be obtained. This result clearly indicates that the carbon deposition is essentially superficial.

Raman spectroscopy was used to investigate the carbon deposition (Fig. 9). The obtained spectrum for hematite after the TPRe with ethanol reached 700 °C does not show any significant bands. On the other hand, after the TPRe at 800 and 900 °C, two bands at ca. 1587 and 1386 cm^{-1} are observed. The first band suggests the formation of graphitic structures and is known as the G band, which is related to tangential vibration modes. The band at ca. 1386 cm^{-1} could be related to defective carbon structures, such as amorphous carbon, which is known as D band [62].

Scanning electron microscopy images of hematite before and after the TPRe at 600, 700 and 900 °C are shown in Fig. 10. It can be observed that the hematite particles (Fig. 10a) exhibit almost no change after treatment at 600 °C (Fig. 10b), except for a slight sintering that produces agglomerated particles. After reaction at 700–900 °C, significant sintering is observed (Fig. 10c). On the other hand, at 900 °C, a high amount of nanometric filaments is observed (Fig. 10d). TEM analyses of this sample (Fig. 11) clearly showed the presence of dense nanometric nuclei. The interplanar distances obtained from the TEM images of 0.200 nm suggested the presence of Fe^o. These particles are covered by a multilayer structure with an interplanar distance of 0.335 nm, suggesting the presence of graphitic structures.

As the metallic iron produced by the reduction with ethanol is to be used to produce H_2 via the oxidation by H_2O, the presence of carbon deposits and Fe_3C are undesirable because they will produce CO, which is a significant poison for fuel cells. For this reason, the reduction of Fe_2O_3 at 700 °C should approximate the best condition to be used for the production of H_2.

Therefore, after the reduction of α-Fe_2O_3 with ethanol at 700 °C, a TPO (temperature programmed oxidation) with H_2O was performed. This oxidation was performed in a classical TPRe system, but instead of monitoring the H_2 consumption by a TCD, the H_2 formation was monitored. The obtained result is shown in the 1st oxidation curve in Fig. 12.

The Fe^o oxidation by H_2O starts at ca. 300 °C, as shown by the two broad peaks centered at 580 °C and 800 °C. According to the Mössbauer and XRD analyses (not shown), when the TPO experiment was interrupted at 700 °C and 900 °C, only Fe^o and

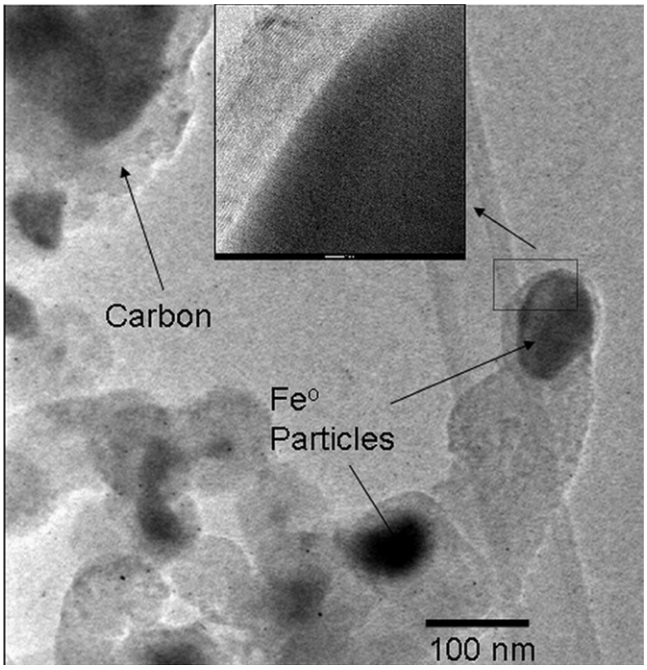

Fig. 11. TEM analysis of hematite (α-Fe_2O_3) after the TPRe with ethanol up to 800 °C.

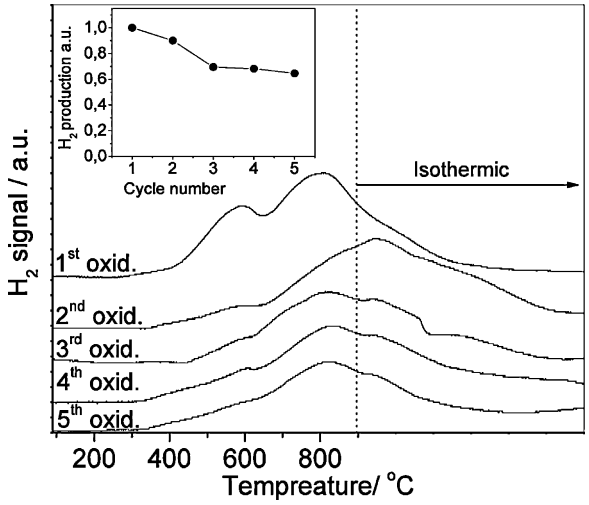

Fig. 12. Hydrogen production curves in the water-oxidation steps after ethanol reduction of α-Fe_2O_3 (at 700 °C) during the five redox cycles (detail: H_2 production in each cycle).

Fe_3O_4 were observed. After the complete TPO experiment, only Fe_3O_4 and traces of Fe_2O_3 could be detected by Mössbauer spectroscopy. These results indicate that the two distinct peaks observed in the 1st oxidation of Fig. 12 are not related to the formation of different phases, but instead are stages in the conversion of Fe^o to Fe_3O_4. Previous work reported that Fe^o is oxidized by H_2O to Fe_3O_4, but not to Fe_2O_3, due to thermodynamic limitations [46,63]. The amount of Fe_2O_3 observed after the complete TPO is likely related to the oxidation of Fe_3O_4 by air at room temperature.

The same oxidized sample was then reduced with ethanol and reoxidized with H_2O (2nd oxidation). A significant difference in the TPO profile can be observed between the 1st and 2nd oxidations, with the first peak almost disappearing and the second peak shifted to higher temperatures. However, in the 3rd, 4th and 5th oxidations, the TPO profile seems to remain similar to the 2nd oxidation.

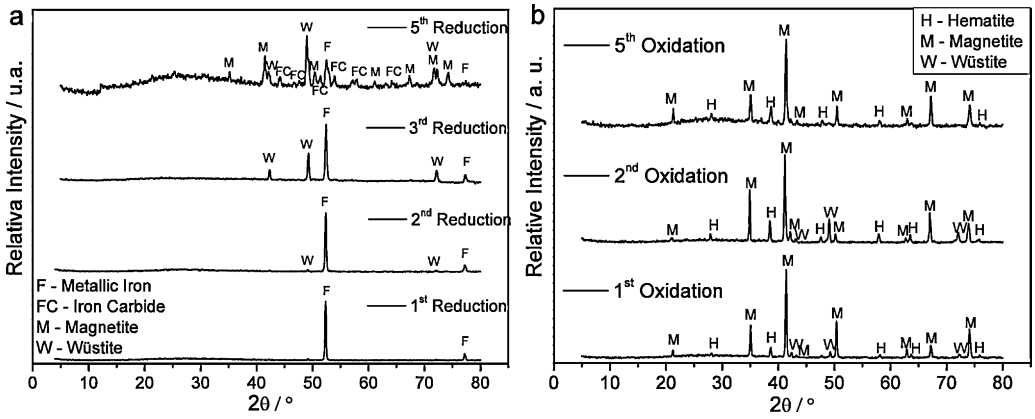

Fig. 13. X-ray diffractograms obtained after multiples steps of reduction with ethanol (a) and oxidation with water (b).

The relative areas of the H_2 signal produced in the five cycles are shown in the detailed image of Fig. 12. It can be observed that in the second and third cycles, the H_2 decreases to ca. 90 and 70%, respectively, of the amount in the first cycle. Although the reasons for this decrease in H_2 production are not clear, it is likely related to sintering and some iron carbide formation in the reduction step. From the 3rd cycle, the system seems to reach some stability, and the H_2 production becomes constant at ca. 70% of the amount produced in the first cycle.

Fig. 13 shows that after the first cycle, the reduction step was not complete, as the iron oxide was reduced to a mixture of metallic iron and wüstite ($Fe_{1-x}O$) (2nd and 3rd cycles). In the 5th reduction, magnetite and iron carbides were also observed. In all the cycles, the oxidation steps mainly promoted the formation of magnetite and small amounts of wüstite and hematite.

4. Conclusion

Different iron oxides, e.g., Fe_2O_3, Fe_3O_4 and γ-FeOOH, can be reduced by ethanol. The iron phases that are subsequently formed are strongly dependent on the reaction temperature. For example, hematite is reduced mainly to magnetite up to 500 °C. At 600 °C, some wustite, $Fe_{1-x}O$, is formed and at 700 °C, mainly Fe^o is formed. At higher temperatures, iron carbide and carbon deposition is observed. Cyclic experiments with consecutive ethanol reduction (at 700 °C) followed by H_2O oxidation showed that some deactivation occurs in the first two cycles, but after the third cycle, the system seems to be stable for consecutive hydrogen production cycles. These results are an important contribution to the development of H_2 production processes based on the use of ethanol and Fe in a redox system. An important advantage of this system is the possibility to store Fe^o and produce H_2 where and when it is necessary.

Acknowledgments

The authors are grateful to CAPES, CNPq and FAPEMIG for financial support.

Appendix A. Supplementary data

Supplementary data associated with this article can be found, in the online version, at doi:10.1016/j.apcatb.2011.11.038.

References

[1] B. Cook, Eng. Sci. Educ. J. 11 (2002) 205–216.
[2] J. Sigurvinsson, C. Mansilla, P. Lovera, F. Werkoff, Int. J. Hydrogen Energy 32 (2007) 1174–1182.
[3] C.M. Stoots, J.E. O'Brien, K.G. Condie, J.J. Hartvigsen, Int. J. Hydrogen Energy 35 (2010) 4861–4870.
[4] T. Kodama, Y. Kondoh, R. Yamamoto, H. Andou, N. Satou, Sol Energy 78 (2005) 623–631.
[5] M. Sakurai, N. Miyake, A. Tsutsumi, K. Yoshida, Int. J. Hydrogen Energy 21 (1996) 871–875.
[6] A. Steinfeld, Sol Energy 78 (2005) 603–615.
[7] M. Ni, M.K.H. Leung, D.Y.C. Leung, K. Sumathy, Renew. Sustain. Energy Rev. 11 (2007) 401–425.
[8] J.H. Yan, Y.R. Zhu, Y.G. Tang, S.Q. Zheng, J. Alloys Compd. 472 (2009) 429–433.
[9] J.N. Armor, Appl. Catal. A: Gen. 176 (1999) 159–176.
[10] D.B. Levin, R. Chahine, Int. J. Hydrogen Energy 35 (2010) 4962–4969.
[11] A. Bedoya, J.C. Castrillon, J.E. Ramirez, J.E. Vasquez, M.A. Zabala, Dyna-Colombia 75 (2008) 137–157.
[12] J.N. Armor, Catal. Lett. 101 (2005) 131–135.
[13] J.M. Ogden, T.G. Kreutz, M.M. Steinbugler, Fuel Cells Bull. (2000) 5–13.
[14] R.M. Navarro, M.C. Alvarez-Galvan, M.C. Sanchez-Sanchez, F. Rosa, J.L.G. Fierro, Appl. Catal. B-Environ. 55 (2005) 229–241.
[15] D. Hotza, J.C.D. da Costa, Int. J. Hydrogen Energy 33 (2008) 4915–4935.
[16] Z.X. Guo, C. Shang, K.F. Aguey-Zinsou, J. Eur. Ceram. Soc. 28 (2008) 1467–1473.
[17] E.M. Gray, Adv. Appl. Ceram. 106 (2007) 25–28.
[18] D.K. Ross, Vacuum 80 (2006) 1084–1089.
[19] M. Benito, J.L. Sanz, R. Isabel, R. Padilla, R. Arjona, L. Daza, J. Power Sources 151 (2005) 11–17.
[20] M. Ni, D.Y.C. Leung, M.K.H. Leung, Int. J. Hydrogen Energy 32 (2007) 3238–3247.
[21] F. Frusteri, S. Freni, L. Spadaro, V. Chiodo, G. Bonura, S. Donato, S. Cavallaro, Catal. Commun. 5 (2004) 611–615.
[22] L.P.R. Profeti, E.A. Ticianelli, E.M. Assaf, Appl. Catal. A: Gen. 360 (2009) 17–25.
[23] S. Cavallaro, V. Chiodo, A. Vita, S. Freni, J. Power Sources 123 (2003) 10–16.
[24] G.A. Deluga, J.R. Salge, L.D. Schmidt, X.E. Verykios, Science 303 (2004) 993–997.
[25] M.H. Youn, J.G. Seo, H. Lee, Y. Bang, J.S. Chung, I.K. Song, Appl. Catal. B-Environ. 98 (2010) 57–64.
[26] S. Velu, K. Suzuki, M. Vijayaraj, S. Barman, C.S. Gopinath, Appl. Catal. B-Environ. 55 (2005) 287–299.
[27] S. Velu, N. Satoh, C.S. Gopinath, K. Suzuki, Catal. Lett. 82 (2002) 145–152.
[28] O. Akdim, W.J. Cai, V. Fierro, H. Provendier, A. Van Veen, W.J. Shen, C. Mirodatos, Top. Catal. 51 (2008) 22–38.
[29] V. Fierro, O. Akdim, H. Provendier, C. Mirodatos, J. Power Sources 145 (2005) 659–666.
[30] J. Kugai, V. Subramani, C.S. Song, M.H. Engelhard, Y.H. Chin, J. Catal. 238 (2006) 430–440.
[31] M.C. Sanchez-Sanchez, R.M. Navarro, J.L.G. Fierro, Catal. Today 129 (2007) 336–345.
[32] M.C. Sanchez-Sanchez, R.M. Navarro, J.L.G. Fierro, Int. J. Hydrogen Energy 32 (2007) 1462–1471.
[33] J.A. Torres, J. Llorca, A. Casanovas, M. Dominguez, J. Salvado, D. Montane, J. Power Sources 169 (2007) 158–166.
[34] M.H. Youn, J.G. Seo, P. Kim, J.J. Kim, H.I. Lee, I.K. Song, J. Power Sources 162 (2006) 1270–1274.
[35] A. Casanovas, J. Llorca, N. Homs, J.L.G. Fierro, P.R. de la Piscina, J. Mol. Catal. a-Chem. 250 (2006) 44–49.
[36] A. Casanovas, C. de Leitenburg, A. Trovarelli, J. Llorca, Chem. Eng. J. 154 (2009) 267–273.
[37] C.P. Rodrigues, V.T. da Silva, M. Schmal, Catal. Commun. 10 (2009) 1697–1701.
[38] C.E.M. Guarido, D.V. Cesar, M.M.V.M. Souza, M. Schmal, Catal. Today 142 (2009) 252–257.
[39] L.V. Mattos, F.B. Noronha, J. Power Sources 152 (2005) 50–59.
[40] R. Padilla, M. Benito, L. Rodriguez, A. Serrano, G. Munoz, L. Daza, Int. J. Hydrogen Energy 35 (2010) 8921–8928.
[41] W.P. Wang, Z.F. Wang, Y. Ding, J.Y. Xi, G.X. Lu, Catal. Lett. 81 (2002) 63–68.
[42] J.R. Salge, G.A. Deluga, L.D. Schmidt, J. Catal. 235 (2005) 69–78.

[43] V. Hacker, R. Fankhauser, G. Faleschini, H. Fuchs, K. Friedrich, M. Muhr, K. Kordesch, J. Power Sources 86 (2000) 531–535.
[44] V. Hacker, J. Power Sources 118 (2003) 311–314.
[45] K. Otsuka, C. Yamada, T. Kaburagi, S. Takenaka, Int. J. Hydrogen Energy 28 (2003) 335–342.
[46] S. Takenaka, K. Nomura, N. Hanaizumi, K. Otsuka, Appl. Catal. A: Gen. 282 (2005) 333–341.
[47] D. Mignard, C. Pritchard, Int. J. Hydrogen Energy 32 (2007) 5039–5049.
[48] M.F. Bleeker, H.J. Veringa, S.R.A. Kersten, Ind. Eng. Chem. Res. 49 (2010) 53–64.
[49] H. Wang, G. Wang, X. Wang, J. Bai, J. Phys. Chem. C 112 (2008) 5679–5688.
[50] M.G. Rosmaninho, L.R. Souza, G.M. Gomes, R.F. Zica, J.S. Nascimento, M.C. Pereira, J.D. Fabris, J.D. Ardison, F.C.C. Moura, R.M. Lago, M.H. Araujo, Hyperfine Interact. 195 (2010) 49–54.
[51] K. Urasaki, N. Tanimoto, T. Hayashi, Y. Sekine, E. Kikuchi, M. Matsukata, Appl. Catal. A: Gen. 288 (2005) 143–148.
[52] X.J. Liu, H. Wang, J. Solid State Chem. 183 (2010) 1075–1082.
[53] H. Wang, X.Q. Feng, X.F. Wang, S.P. Cheng, S.L. Gao, Int. J. Hydrogen Energy 33 (2008) 7122–7128.
[54] R.M. Cornell, U. Schwertmann, The Iron Oxides, VCH, 1996.
[55] F.C.C. Moura, G.C. Oliveira, M.H. Araujo, J.D. Ardisson, W.A.A. Macedo, R.M. Lago, Appl. Catal. A: Gen. 307 (2006) 195–204.
[56] L.C.A. Oliveira, J.D. Fabris, R.R.V.A. Rios, W.N. Mussel, R.M. Lago, Appl. Catal. A: Gen. 259 (2004) 253–259.
[57] T. Kendelewicz, P. Liu, C.S. Doyle, G.E. Brown, Surf. Sci. 469 (2000) 144–163.
[58] F. Magalhaes, M.C. Pereira, J.D. Fabris, S.E.C. Bottrel, M.T.C. Sansiviero, A. Amaya, N. Tancredi, R.M. Lago, J. Hazard. Mater. 165 (2009) 1016–1022.
[59] F.J. Perez-Alonso, M.L. Granados, M. Ojeda, T. Herranz, S. Rojas, P. Terreros, J.L.G. Fierro, M. Gracia, J.R. Gancedo, J. Phys. Chem. B 110 (2006) 23870–23880.
[60] F. Bonnet, F. Ropital, P. Lecour, D. Espinat, Y. Huiban, L. Gengembre, Y. Berthier, P. Marcus, Surf. Interface Anal. 34 (2002) 418–422.
[61] K.F. Tan, J. Xu, J. Chang, A. Borgna, M. Saeys, J. Catal. 274 (2010) 121–129.
[62] T. Belin, F. Epron, Mater. Sci. Eng. B-Solid State Mater. Adv. Technol. 119 (2005) 105–118.
[63] K. Otsuka, T. Kaburagi, C. Yamada, S. Takenaka, J. Power Sources 122 (2003) 111–121.